Revealing operando reconstruction effect of Ni-Co dual-cation in black phosphorus for promoting oxygen evolution reaction

Zhao, M; Zhang , R; Fu, ZM; Xiao, H; Bai, M; Zhang, L; Zhang, JM; Jia , JF & YANG, Nianjun (2024) Revealing operando reconstruction effect of Ni-Co dual-cation in black phosphorus for promoting oxygen evolution reaction. In: INTERNATIONAL JOURNAL OF HYDROGEN ENERGY, 53 , p. 263 -272.

DOI: 10.1016/j.ijhydene.2023.12.084
Handle: http://hdl.handle.net/1942/42242

Revealing operando reconstruction effect of Ni-Co dual-cation in black phosphorus for promoting oxygen evolution reaction

Man Zhao[a,†], Rong Zhang[a,†], Zimei Fu[a], He Xiao[a,*], Meng Bai[a], Li Zhang[a], Junming Zhang [a], Jianfeng Jia[a,*] and Nianjun Yang[b,c*]

[a] Key Laboratory of Magnetic Molecules & Magnetic Information Materials Ministry of Education, The School of Chemical and Material Science, Shanxi Normal University, Taiyuan 030000, China

[b] Department of Chemistry, Hasselt University, 3590 Diepenbeek, Belgium

[c] IMO-IMOMEC, Hasselt University, 3590 Diepenbeek, Belgium

*Corresponding author

E-mail: xiaohe200808@sxnu.edu.cn (H, Xiao); jiajf@dns.sxnu.edu.cn (J.F. Jia); nianjun.yang@uhasselt.be (N. Yang)

Author contributions

† These authors made equal contribution.

ABSTRACT

Sluggish reaction kinetic and large overpotential of the oxygen evolution reaction (OER) result in low energy efficiencies of different OER related devices. To solve these challenges, an OER electrocatalyst is constructed by coupling black phosphorus with Co/Ni nanosheets during a facile electrolysis-solvothermal process, where the bulky BP is successfully exfoliated into BP sheets (BP NSs) and the Co or Ni precursors are generated via anodic oxidation. Then, BP sheets are combined with Co-Ni species and finally formed into Co-Ni/BP composite via subsequent solvothermal process. The OER tests on this composite show the overpotential is 292 mV at 10 mA cm^{-2}, much lower than that (341 mV) on a RuO_2 catalyst. The TOF value of this composite is 0.71 s^{-1} at 1.8 V (*vs*. RHE), 14.2 times higher than that of

Co/BP (0.05 s^{-1}) and 23.7 times higher than Ni/BP (0.03 s^{-1}). Operando structure characterizations of this composite reveal that Co^{2+}-Ni^{2+} dual-sites are formed on Co-Ni/BP and electrons are transferred from Ni to Co *via* a P bridge. These Co^{2+}-Ni^{2+} dual-sites evolve into Co^{3+}-Ni^{3+} dual-sites during the OER, where Ni_2P is formed into NiOOH and CoP turns into Co_3O_4. The Ni-P_x-Co bridge is finally transformed into a heterogeneous Co_3O_4/NiOOH structure. This heterostructure efficiently regulates electronic structure of Co and Ni sites, resulting in the favorable adsorption of OH*, conversion of rate-determining step, reduced activation energy of the whole reaction, and eventually enhanced intrinsic activity toward the OER. This work provides a guidance to explore operando reconstruction mechanism of black phosphorus based electrocatalysts during electrocatalytic reactions.

KEYWORDS: Electrolytic synthesis, Oxygen evolution reaction, Reconstruction effect, Ni-Co dual-cation, Black phosphorus

1. Introduction

The oxygen evolution reaction (OER) is well-known to feature sluggish reaction kinetics and large overpotentials, leading to energy loss and eventually low energy efficiencies of different electrochemical technologies such as rechargeable metal-air batteries, water splitting devices, and unitized regenerative fuel cells. To promote the OER kinetics, numerous electrocatalysts have been designed and synthesized together with different catalyst supports [1–6]. With respect to widely utilized supports, black phosphorus (BP) is chosen owing to its high surface area and high carrier mobility [7–9]. As for catalysts, Fe group metals (e.g., Fe, Co, Ni) have been extensively employed, due to their unique *d*-orbital structures [10–16]. The coupling of Fe group metals with black phosphorus is thus expected to obtain efficient OER electrocatalysts.

On the other hand, reconstruction phenomenon has been noticed during the electrocatalytic reactions [17–24]. Reconstruction of a pre-catalyst makes a crucial effect on intrinsic properties and electrical structures of catalytic materials, which directly decide the energy barrier and kinetics of studied catalytic reactions [25–30]. In this context, the investigation of original reconstruction is important to comprehend reconstruction processes. Reconstruction phenomena of a catalysts might be possible even during the OER. This is because oxygenic intermediates are inevitably generated on the electrocatalysts during this process, especially for nonprecious metal materials. Such structural evolutions are recognized to proceed preferably towards superior reaction-states. Meanwhile, the stability performance of such reconstructed species

might be promoted.

Taking black phosphorus-based materials as the example, they are easily oxidized due to their active lone electrons in the surface. Their reconstruction, especially for during the OER is thus susceptible [7,31]. For example, two-dimensional (2D) materials, namely BP nanosheets and $Ni(OH)_2$ nanosheets have been combined for the promoted OER [31]. The as-obtained overpotential on this catalyst was 297 mV at 10 mA cm^{-2}. The reconstruction phenomena of this catalyst were revealed by use of theoretical calculation and experimental methods. Surface oxidization of BP nanosheets into P-OH was found together with phase conversion of $Ni(OH)_2$ nanosheets into NiOOH oxyhydroxide at the initial reconstruction stage. Such a reconstruction process greatly reduced the overpotential of the OER or enhanced kinetics of the OER. It has to highlight here that the study of reconstruction process of an electrocatalyst or to reveal the change of surface composition and structure of an electrocatalyst is benefit to reveal real active sites and catalytic mechanisms of different reactions. Surface reconstruction of an electrocatalyst is expectedly regulated to create its more active sites and eventually improve its catalytic activity. For example, the reconstructed interface of a heterostructure accelerates proton/electron transfer and product separation, reduces activation energy barrier, and further improves the intrinsic activity for the OER. Surprisingly, the studies about such reconstruction mechanisms are rare in the literature.

As for traditional synthesis methods, BP NSs and Co-Ni species are synthesized individually. To reduce preparation processes, a facile three-electrode (single

cathode-double anodes) system is constructed to synthesize Co-Ni/BP hybrid (Co–Ni/BP). Here, we couple the hybrid of black phosphorus nanosheets with Co-Ni (Co-Ni/BP) by use of a simple three-electrode method. The surface reconstruction mechanism of this Co-Ni/BP catalyst is revealed using different characterization techniques. The reconstruction effect on the reaction mechanism of the OER is systematically studied, including adsorption of intermediators, activation energies, and the rate-determining step during the OER. A synergistic catalytic mechanism of Ni-Co dual-cation is also proposed.

2. Experimental

2.1 Chemicals and materials

Bulky BP was purchased from Kunming Black Phosphorous Company (China). A nickel wire and a cobalt wire were bought from Runde Metal Material Company (China). Chemicals such as tetrabutylammonium trifluoromethanesulfonate ($TBACF_3SO_3$, 99%) and propylene carbonate (PC, 99.9%) were bought from Aladdin.

2.2 Preparation of Co-Ni/BP heterostructures

Here three-electrode method was used to synthesize these black phosphorus-based samples. Bulky black phosphorus was served as cathode while cobalt wire and nickel wire were both supported as anodes. These three electrodes were immersed in PC solvent containing 0.1 M $TBACF_3SO_3$. This electrolysis experiment was carried out at the voltage of 30 V. This nickel wire was electrolyzed

for 30 min, then this nickel wire anode was replaced by two cobalt wires electrolyzed for another 30 min. These exfoliated BP sheets were taken out from cathode and dispersed into electrolyte solution. This obtained solution was ultrasounded in an ice water bath for 2 h. Then this mixed solution was transferred to an 80 mL Teflon-lined container for solvothermal treatment at 160 °C in the Ar atmosphere for 12 h. The obtained composite was washed with PC solvent and ethanol, then dried at 60 °C for 6 h. This obtained composite is defined as Co-Ni/BP. For comparison, these catalysts prepared only using cobalt wire anode or nickel wire anode are defined as Co/BP and Ni/BP, respectively.

2.3 Materials characterization

Crystalline phase analysis of different samples was conducted using an X-ray diffractometer (Ultima IV-185) with Cu Kα radiation. The oxidation states and chemical composition of as-prepared samples were examined by use of X-ray photoelectron spectroscopy (XPS, Thermo Fisher Scientific) applying an Al Kα X-ray source. The morphologies and structures of as-prepared samples were measured with high-resolution transmission electron microscopy (HRTEM), transmission electron microscopy (TEM), and scanning electron microscopy (SEM) on the FEI Tecnai F20 and JSM-7001F, respectively.

2.4 Electrochemical measurements

The OER performance of as-prepared samples were tested in 1 M KOH solution on a

CHI 660E electrochemical workstation (CH Instruments, Inc., Shanghai, China). In a traditional three-electrode system, working electrode, counter electrode and reference electrode were a glassy carbon electrode (GCE, 3 mm in diameter), a graphite rod, and a Hg/HgO electrode, respectively. To load an electrocatalyst, 5 μL of its ink was coated on the GCE. The overpotential was measured by means of linear sweep voltammetry within the potential range from 0 to 1 V (*vs*. Hg/HgO) at a scan rate of 5 mV s^{-1}. The Tafel plots were re-plotted based on as-obtained linear sweep voltammograms (LSVs) and the Tafel equation. The electrochemical impedance spectroscopy (EIS) was carried out within a frequency range from 10^5 to 1 Hz at a current density 10 mA cm^{-2}. All potentials in this work were converted into reversible hydrogen electrode (RHE) using the equation of $E_{RHE} = E_{Hg/HgO} + 0.059\ pH + E^{\theta}_{Hg/HgO}$.

3. Results and discussion

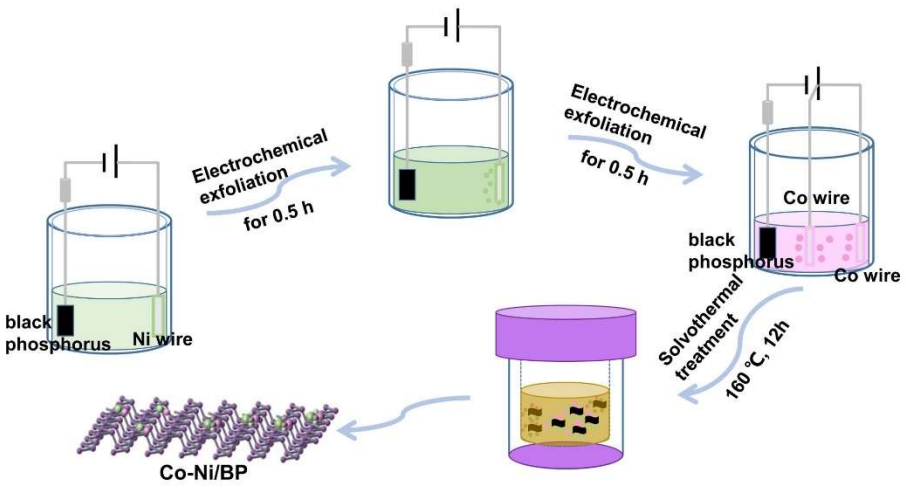

Fig. 1 Schematic of the preparation process for Co-Ni/BP.

Here the Co-Ni/BP composite was synthesized via a facile

electrolysis-solvothermal process (**Fig. 1**). In the first electrolysis process, the bulky BP is exfoliated into BP sheets (BP NSs) while the Co or Ni precursors are formed via anodic oxidation. The BP NSs are coupled with Co-Ni species and finally formed into Co-Ni/BP composite via the second solvothermal process. As is expected, this method not only offers high-surface area supporter via exfoliation process, but also constructs multivalence Co-Ni dual-cations for OER.

The morphology and nanostructures of as-prepared samples were firstly investigated with transmission electron microscopy (TEM) and high-resolution TEM (HRTEM). It's seen that the raw bulky BP shows the morphology of thick blocky structure (**Fig. S1**). Via the electrochemical exfoliation, the obtained BP NSs display much thinner lamellar structure (**Fig. 2a**). Moreover, the surface of these BP NSs is smoothy before OER tests. Their crystal plane of (040) possesses an interplanar distance of 0.263 nm (**Fig. 2b**). Different from BP NSs, more irregular aggregations are formed over Ni/BP (**Fig. 2c**). From the HRTEM images of Ni/BP catalyst (**Fig. 2d**-**2e**), it's found the emerging lattice fringe spacings are 0.192 and 0.155 nm, well match with (210) plane of Ni_2P and (300) of $Ni(OH)_2$, respectively. They verify the successful formation of Ni_2P and $Ni(OH)_2$ over the Ni/BP catalyst. For the Co/BP catalyst (**Fig. 2f**), low-crystalline aggregates are dispersed on lamellar BP nanosheet. Its lattice fringe spacings of 0.245 nm and 0.200 nm are associated with the (101) plane of the CoO and (210) plane of the CoP (**Fig. 2g-2h**), respectively. Similar to Ni/BP and Co/BP, Co-Ni/BP also displays the low-crystalline aggregated morphology, indicating decreased crystallinity due to introduction of Co/Ni (**Fig. 2i**). Inferred from

HRTEM images of Co-Ni/BP catalyst (**Fig. 2j-2l**), the (101) plane of CoO, the (200) plane of CoP, the (110) plane of $Ni(OH)_2$ and the (201) plane of Ni_2P are identified, indicating both Co species and Ni species are co-loaded on the BP NSs, solidly confirming the formation of the Co-Ni/BP catalyst.

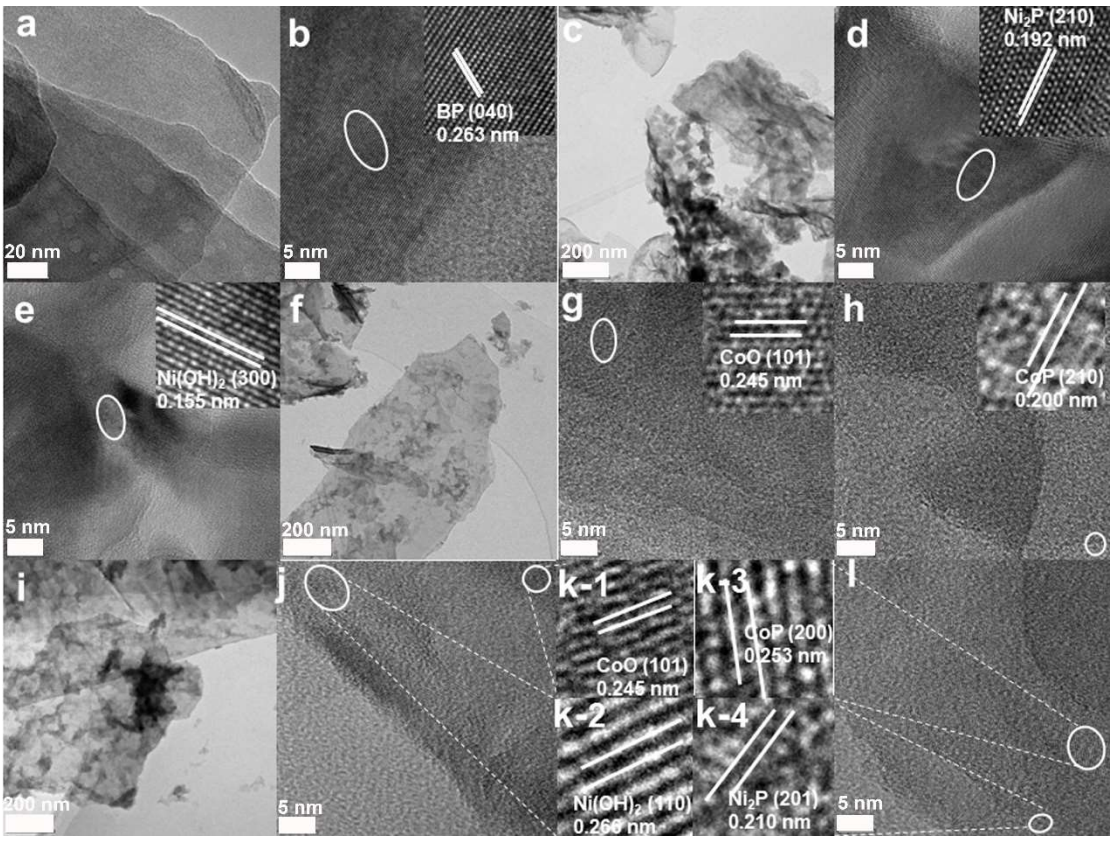

Fig. 2 (a) Representative TEM image and (b) representative HRTEM image of BP NSs; (c) representative TEM and (d,e) HRTEM images of the Ni/BP catalyst; (f) representative TEM and (g,h) HRTEM images of the Co/BP catalyst; (i) representative TEM and (j,k-1,k-2,k-3,k-4,l) HRTEM images of the Co-Ni/BP catalyst.

To identify the oxidation states of as-prepared catalysts, their cyclic voltammograms (CVs) were recorded and related oxidation-reduction peaks were

analyzed. In the CV curve of the Co/BP catalyst, an oxidation peak of Co^{2+} to Co^{3+} appears at 1.22 eV (**Fig. 3a**), while the CV curve of the Ni/BP catalyst shows an oxidation peak of Ni^{2+} to NiOOH (Ni^{3+}) at 1.50 V (**Fig. 3b**). Compared the peaks of the Co-Ni/BP catalysts with those of the Co/BP catalyst or the Ni/BP catalyst (**Fig. 3c**), an obvious shift of oxidation peak potential is found. For the Co-Ni/BP catalyst, the Co^{2+}-to-Co^{3+} peak positively shifts by 0.7 V, while the Ni^{2+}-to-NiOOH peak negatively shift by 0.4 V. These results indicate the formation of a new Ni-Co structure rather than single Ni or Co structure. No peak belonging to BP is observed, because this formed peak is assigned to oxidation peak of metal (**Fig. S2**). Noticeably, operando reconstruction phenomenon was observed in the Co-Ni/BP catalyst (**Fig. 3d**). This is because the oxidation peaks of both Co^{2+}-to-Co^{3+} and Ni^{2+}-to-NiOOH almost disappear only after the first cycle. It is thus assumed that the original structure of the Co-Ni/BP catalyst mainly shows the Co^{2+}-Ni^{2+} dual-sites, which evolve into Co^{3+}-Ni^{3+} dual-sites together with the occurrence of oxidation reactions of metal centers. In other words, both Co^{3+} and Ni^{3+} are real active sites for the observed electrocatalytic OER. The interaction between Co^{3+} and Ni^{3+} is further expected to efficiently adjust the electron structure of Co-Ni dual active sites on the Co-Ni/BP catalyst.

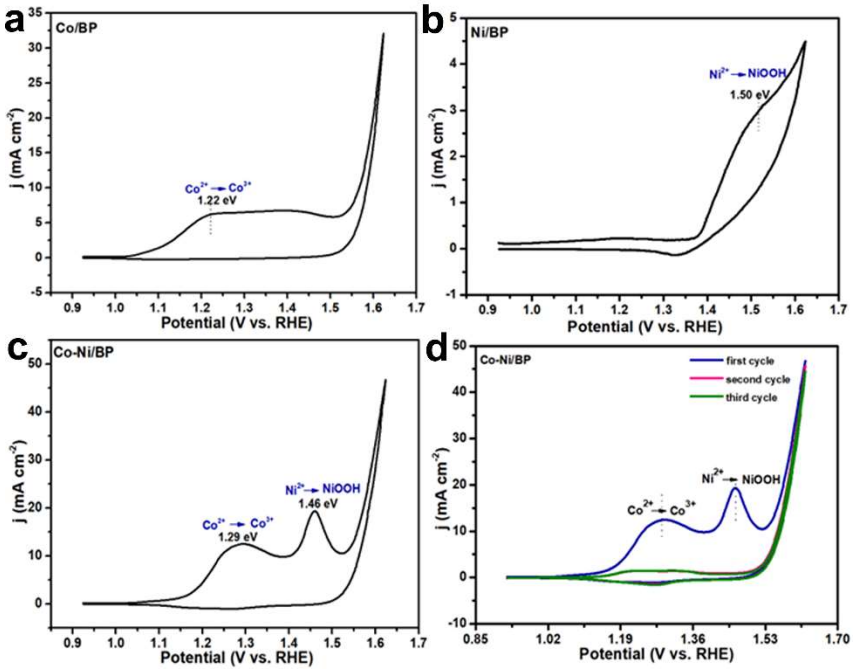

Fig. 3 One single cyclic voltammogram of the (a) Co/BP, (b) Ni/BP, and (c) Co-Ni/BP catalysts; (d) three cycles of the Co-Ni/BP catalyst. The electrolyte is 1.0 M KOH and the scan rate is 10 mV s^{-1}.

To obtain the structural details of the BP, Ni/BP, Co/BP and Co-Ni/BP, their XRD patterns were recorded and compared (**Fig. S3**). In the XRD spectrum of BP, three main characteristic peaks are located at 16.9º, 34.1º, and 52.3º. They are assigned to the (020), (040), (060) planes of BP, respectively (*PDF#73-1358*). The small peaks at 26.4º, 35.0º, 40.0º, 43.0º, 50.8 º, 55.8º, 56.7º are assigned to (021), (111), (041), (131), (112), (200), and (132) of BP. Despite of characteristic peaks assigned to BP, Ni/BP shows three peaks at 40.6º, 44.5º and 47.3º, corresponding to (111), (021), (210) of Ni_2P (*PDF#65-3544*). This indicates Ni_2P is formed on Ni/BP. Different from Ni/BP, as for Co/BP and Co-Ni/BP, there are no obvious diffraction peaks corresponding to cobalt or nickel species. It can be thus concluded that the

Co-Ni/BP mainly displays the phase of BP and crystallinity of formed nickel or/and cobalt species is extremely low, which is probably due to amorphous doping, minimal size or mixcrystal structure.

To reveal as-discussed oxidation states, electron structures and reconstruction phenomenon, these catalysts were examined by means of XPS. In the XPS survey spectrum of these as-prepared catalysts (**Fig. S4**), the presence of Ni, Co, O and P elements are confirmed. In the Co 2p XPS spectrum of the Co/BP catalyst (**Fig. 4a**), the characterization peaks are located at 778.7 and 793.5 eV. Moreover, the CoO_x species, including Co^{3+} (781.3 and 797.2 eV) and Co^{2+} (783.1 and 799.0 eV) are distinguished. In the XPS spectrum of the Co-Ni/BP catalyst, the XPS peaks of CoO_x species almost remain the original positions in comparison with those of the Co/BP catalyst, while the peaks of CoP negatively shift. This indicates that the Co species gain more electrons than the Ni species. Meanwhile, in the Ni 2p XPS spectra of the Ni/BP and Co-Ni/BP catalyst (**Fig. 4b**), the peaks of both Ni(II) species and NixP species are seen. The incorporation of Co into the Ni/BP catalyst is then expected to make the binding energy of NixP in the Co-Ni/BP catalyst shift towards a higher value. Namely, electrons are transferred out from the Ni species. Different from obvious variation of the NixP species, the Ni(II) species on the Co-Ni/BP catalyst almost remain their original structure. The high-resolution P 2p XPS spectra of these catalysts were also recorded, including BP NSs as well as the Co/BP, Fe/BP and Co-Fe/BP catalysts (**Fig. S5**). For BP NSs, three peaks are present at 129.8, 130.6, and 133.6 eV, which are assigned to P $2p_{3/2}$, P$2p_{1/2}$, and P–O, respectively. While the

binding energies of P 2p in the Co/BP, Fe/BP and Co-Fe/BP catalysts are shifted toward lower binder energies when compared with that of BP NSs, indicating strong electron interactions between Co (or Fe) and BP. Except the peaks of P $2p_{3/2}$, $P2p_{1/2}$ and P-O species, P-metal (P-M) peak is also found and fitted. As observed, this fitted P-M peak (129.2 eV) in Co-Ni/BP is just present at the medium position between Co/BP (129.0 eV) and Ni/BP (129.4 eV). Combining P 2p XPS spectra with Co 2p XPS spectra as well as Ni 2p XPS spectra, it's concluded that Co-P-Ni interfacial species are generated. Electron migration from Ni to Co along the way of P bridge via the interface, could effectively regulate the electronic structure, which in turn optimizes the adsorption and enhances electrochemical behavior of Co-Ni/BP. Such BP interfacial charge transfer is also observed in BP-based compound[32–36].

Such a metal interaction or the Ni-P_x-Co structure was then verified by analyzing the Raman spectra of BP, Ni/BP, Co/BP and Co-Ni/BP. In the Raman spectrum of BP NSs (**Fig. 4c**), three vibration bands appear at about 361.5, 438.3, and 466.9 cm^{-1}. They correspond to the out-of-plane A^1_g mode, in-plane B_{2g} and A^2_g vibration modes, respectively [8,37–39]. In comparison with the peaks of BP NSs, those of the Ni/BP, Co/BP and Co-Ni/BP catalysts are negatively shifted. It is probably caused by the electron transfer between the Co (Ni) species and BP. Noticeably, the A^2_g peak of the Co-Ni/BP catalyst is just present between that of Ni/BP catalyst and Co/BP catalyst. This indicates the bonding strength of formed P-metal is between P-Co and P-Ni. That's to say, Ni-P-Co structure is generated, as already demonstrated from XPS results of the Co-Ni/BP catalysts.

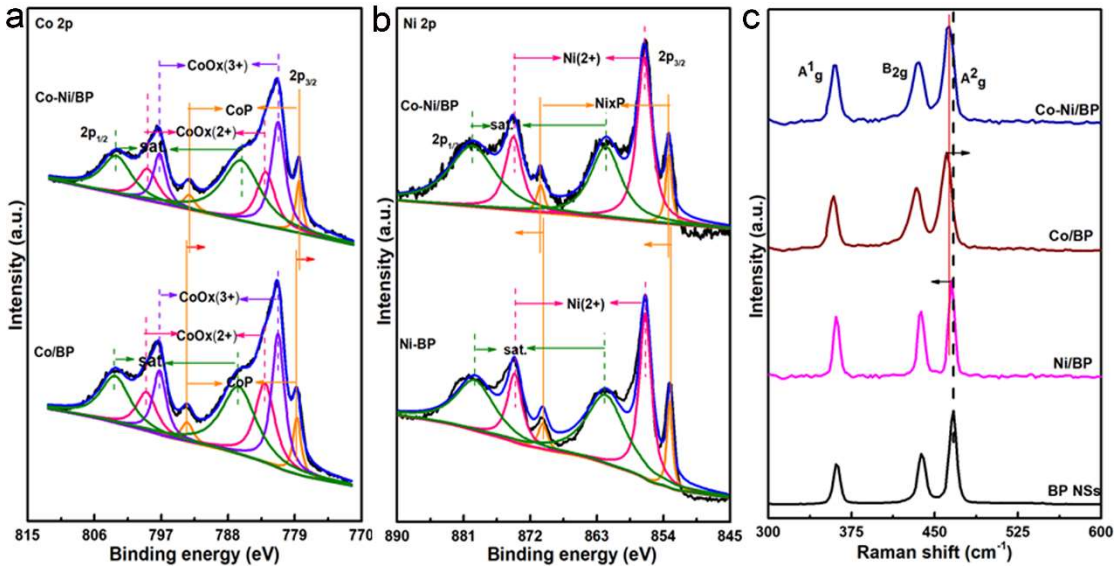

Fig. 4 (a) Co 2p XPS spectra of the Co-Ni/BP and Co/BP catalysts; (b) Ni 2p XPS spectra of the Co-Ni/BP and Ni/BP catalysts;(c) Raman spectra of the Co-Ni/BP, Co/BP, Ni/BP and BP NS catalysts.

The composition of the Co-Ni/BP catalyst was optimized by applied different electrolysis voltages (**Fig. S6**) and electrolysis times (**Fig. S7**). The OER performance of these Co-Ni/BP composites was further tested. The best Co-Ni/BP composite that was synthesized using an electrolysis voltage of 30 V and an electrolysis time of 30 min shows the overpotential of 292 mV (without *iR* compensation) at 10 mA cm^{-2}, superior to that (341 mV) of the typical OER catalyst - RuO_2. This obtained Co-Ni/BP also displays competitive electrocatalytic activity towards alkaline OER in comparison with BP-based materials (**Table S1**) [7,8,31,37,39,40]. To reveal component synergy of Co and Ni, the linear sweep voltammograms (LSVs) of BP NSs, Ni/BP and Co/BP catalysts were recorded in 1 M KOH (**Fig. 5a**). The overpotentials at 10 mA cm^{-2} (without *iR* compensation) follows the order of Co-Ni/BP (292 mV) < Co/BP (365 mV) < Ni/BP (380 mV) < BP NSs (> 500 mV)

(**Fig. 5b**). This indicates that both Co species and Ni species contribute to the OER activity of as-synthesized catalysts. The Co species seems to exhibit higher OER performance than Ni species.

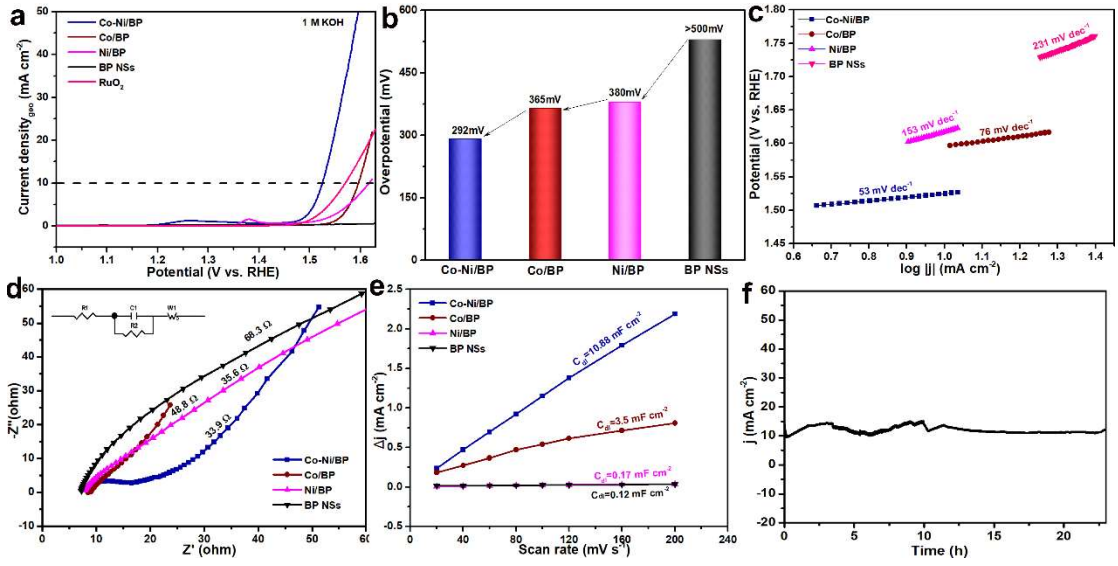

Fig. 5 (a) Linear sweep voltammograms, (b) Overpotential comparison, (c) Tafel plots, (d) Nyquist plots and (e) C_{dl} values of BP NSs, Ni/BP, Co/BP, Co-Ni/BP catalysts in 1 M KOH; (f) Chronoamperometric curve of Co-Ni/BP catalyst at the constant potential of 1.52 V.

The Tafel analysis was then applied to ensure the rate-determining step (RDS) of this alkaline OER on these catalysts. It is known that the evolution of OH^- into O_2 contains a multistep reaction process: a) a Tafel slope of 120 mV dec^{-1} indicates that the RDS is the first electron transfer process; b) a Tafel slope of 60 mV dec^{-1} indicates that the RDS is the second chemical reaction process; c) a Tafel slope of 40 mV dec^{-1} suggests that the electron–proton reaction is the RDS[7]. In our study, the Tafel slopes for the Ni/BP and Co/BP catalysts are 153 and 76 mV dec^{-1} (**Fig. 5c**) respectively. The

Tafel slope of the Co-Ni/BP catalyst is only 53 mV dec^{-1}. Consequently, the RDS of the OER on the Ni/BP and Co/BP catalysts has been transferred from an electron transfer process or a chemical reaction process to an electron-proton reaction on the Co-Ni/BP catalyst. Thus, electron–proton reaction process (formation of HOO*) is considered as the RDS over Co-Ni/BP catalyst. The RDS conversion of the this alkaline OER confirms the promotion of electron transfer and the optimized adsorption properties of the Co-Ni/BP catalyst. Such electron-transfer properties of these catalysts were further verified from their Nyquist plots (**Fig. 5d**) since the Co-Ni/BP catalyst shows smaller radius in the semicircle of its Nyquist plot than both Ni/BP and Co/BP catalysts. Further analysis of the impedance data is carried out by taking a fitting based on the Randles circuit to obtain the charge-transfer resistance values. The R_{ct} value is 33.9 Ω for Co-Ni/BP, lower than that of BP NSs (68.3 Ω), Ni/BP (35.6 Ω) and Co/BP (48.8 Ω). This indicates that both Ni and Co promote the rates of electron transfer, leading to enhanced OER performance of the Co-Ni/BP catalyst. Namely, both Ni and Co promote the rates of electron transfer, leading to enhanced OER performance of the Co-Ni/BP catalyst.

To further support this statement, the component synergy of the Co-Ni/BP was investigated, namely the comparison of electrochemically active surface areas (ECSAs) of the studied catalysts. The electrochemical double-layer capacitances (C_{dl}) of different catalysts (**Fig. 5e**) were calculated from their cyclic voltammograms that were recorded within non-faradaic domains at different scan rates (**Fig. S8**). The Co-Ni/BP catalyst possesses a C_{dl} value of 10.88 $mFcm^{-2}$, higher than those of both

Ni/BP (0.17 $mFcm^{-2}$) and Co/BP (3.5 $mFcm^{-2}$) catalysts. In other words, the Co-Ni/BP catalyst is expected to exposes more active sites than both Ni/BP and Co/BP catalysts, leading to its enhanced OER performance. In addition, these obtained ECSA-normalized current densities of different samples are shown in Fig. **S9**. It's seen that Ni/BP shows the highest ECSA-normalized current density among these samples, due to its lowest ECSA. While for Co-Ni/BP, it displays higher ECSA-normalized current density than Co/BP and BP. The Co-Ni/BP catalyst exhibits high stability during the OER, as confirmed from a chronoamperometric test for 23 h (**Fig. 5f**). Noticeably, as the reaction goes on, the current is enhanced when compared with its initial current, probably due to an activation process of the Co-Ni/BP catalyst.

The XPS technique was further applied to uncover the reconstruction of Co-Ni/BP during the OER, namely the variation of oxidation states of the Ni and Co species before and after the OER. In the Co 2p (**Fig. 6a**) and Ni 2p (**Fig. 6b**) XPS spectra after the OER test, both NixP peak and CoP peak disappear, while the amounts of both Ni^{3+} and Co^{3+} species increase. Combining with the voltametric results, it can be inferred that either Ni or Co in the original Ni-Px-Co structure is present with an oxidation valence of 2+, namely a Ni^{2+}-Px-Co^{2+} structure. After the OER test, NixP is oxidized into NiOOH while CoP turns into CoOx. Finally, a heterogeneous structure of CoOx-NiOOH is formed.

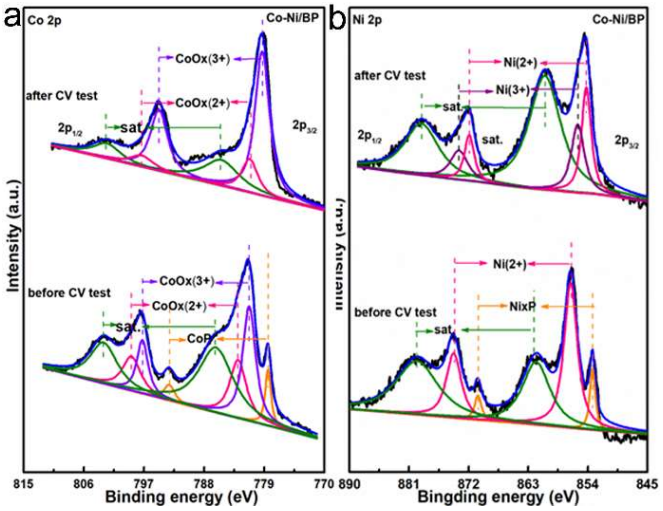

Fig. 6 (a) Co 2p XPS spectra and (b) Ni 2p XPS spectra of the Co-Ni/BP catalysts before and after the CV test.

To further reveal evolution process of Co species and Ni species after the OER, the TEM and HRTEM analysis of the studied catalysts was carried out. TEM image (**Fig. 7a**) of Co-Ni/BP catalyst suggests oxidation process intensifies the aggregation of surface species. In the HRTEM images of the Co-Ni/BP catalyst (**Fig. 7b-7e**), the generation of more crystalline phases of Co_3O_4 and NiOOH is found or a heterostructure of Co_3O_4-NiOOH is formed. From the view of thermodynamic stability, the corresponding oxides or (oxy)hydroxides are the most stable states under oxidation conditions. This formed heterostructure of Co_3O_4-NiOOH is thus expected to efficiently adjust electronic structures of both Co sites and Ni sites, then optimize the adsorption performance of the Co-Ni/BP catalyst, and finally boost its OER performance. Moreover, HAADF-STEM image of the Co-Ni/BP catalyst after the OER test (**Fig. 7f**) and corresponding elemental mapping images (**Fig. 7g-7j**) suggest uniform distribution of P, Ni, Co and O elements, demonstrating the unform formation of the CoNi species on the BP NSs, consistent with XPS results.

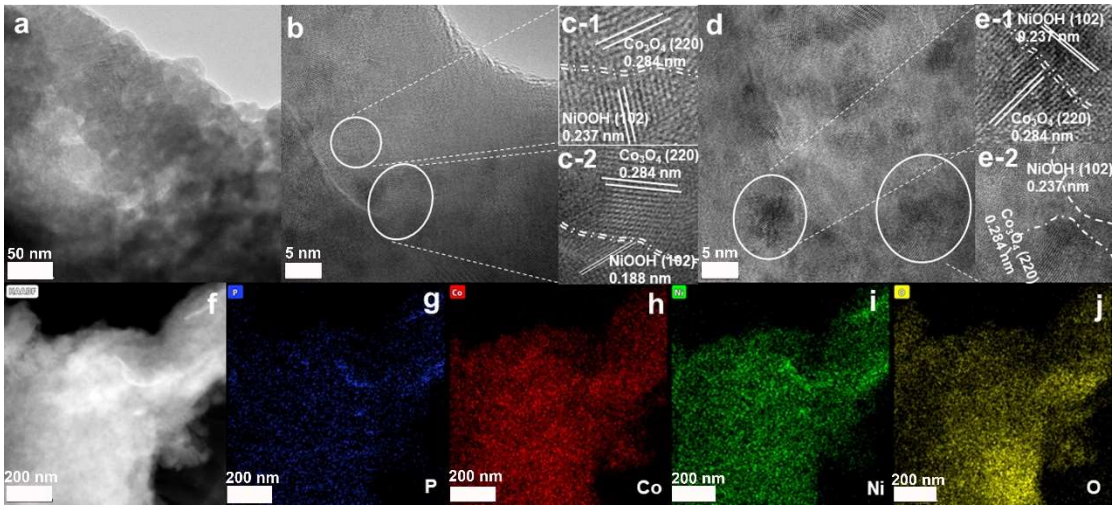

Fig. 7 (a) Representative TEM and (b,c-1,c-2,d,e-1,e-2) HRTEM images of the Co-Ni/BP catalyst after the OER test at different resolutions; (f) HAADF-STEM image and (g-j) EDS mapping images of the Co-Ni/BP catalyst.

It is known that the adsorption of OH^- and subsequent formation of OH* is the initial step in the complicated OER process. The bonding strength of absorbed OH* over these obtained catalysts subsequently decides the formed oxygen intermediates (e.g., O* and OOH*) and the whole OER performance [10,12,41,42]. In other words, a desired OER catalyst must own a favorable bonding strength of OH*. On the other hand, the amount of OH* is possible to be detected by methanol oxidation reaction (MOR) under the same condition for the OER. This is because the OH* intermediate is electrophilic and can be detected by nucleophiles such as methanol molecule [43,44]. The degree of surface OH* coverage can be reflected in the form of the current difference that is resulted from MOR and OER, which further expresses the OH* adsorption ability. In our case (**Fig. 8**), the current difference (filled area) decreases as follows: $S_{Co/BP}$ (6.30) > $S_{Co\text{-}Ni/BP}$ (5.82) >$S_{Ni/BP}$ (0.78) > $S_{BP\ NS}$ (0.031), demonstrating that the adsorption strength toward OH* varies in the trend: Co/BP > Co-Ni/BP > Ni/BP > BP NS. Noticeably, introduction of Co or Ni to BP strengthens the OH* adsorption and

the adsorption strengthen of Co site is stronger than that of Ni site. Among these obtained catalysts, the Co-Ni/BP catalyst exhibits the appropriate adsorption of OH*, leading to its improved catalytic OER performance.

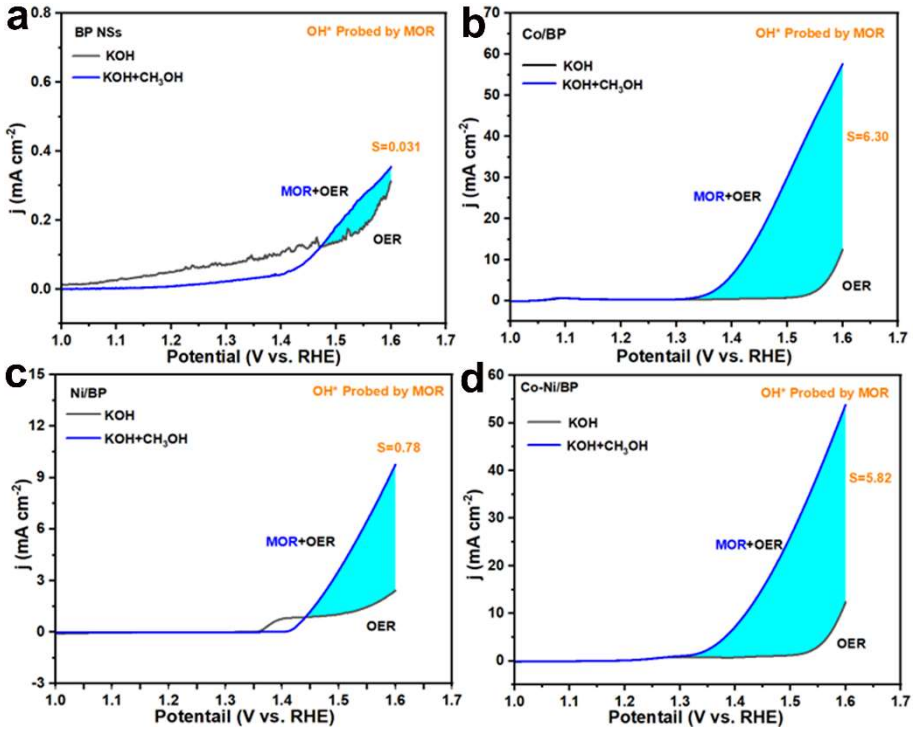

Fig. 8 LSVs of oxygen intermediates during methanol oxidation on BP NSs (a), Co/BP (b), Ni/BP (c) and Co-Ni/BP in 1 M KOH (black) and 1 M KOH + CH_3OH (purple) at a scan rate of 50 mV s^{-1}. These filled areas are the current difference that is caused by MOR.

The activation energy (E_a) for the OER on the Co-Ni/BP catalyst was also estimated (**Fig. 9**), since it is an intrinsic indicator to describe catalytic activity of a catalyst. With aid of Arrhenius equation, the E_a value was calculated by analyzing LSVs recorded at different temperatures (**Fig. S10**) [45]. The E_a value of the Co-Ni/BP catalyst is 35.36 kJ mol^{-1}, much lower than that of the Co/BP catalyst

(45.05 kJ mol^{-1}), the Ni/BP catalyst (49.71 kJ mol^{-1}), and the BP NS catalyst (56.21 kJ mol^{-1}). These values demonstrate that the water oxidation kinetics on the Co-Ni/BP catalyst is substantially improved. The intercomponent synergy significantly alters the intrinsic properties of this catalyst. The turnover frequency (TOF) value of the Co-Ni/BP catalyst toward the OER is 0.71 s^{-1} at 1.807 V (vs. RHE), more than that of the Co/BP catalyst (0.05 s^{-1}) and the Ni/BP catalyst (0.03 s^{-1}). The constructed heterostructure of Co_3O_4-NiOOH thus effectively improves the intrinsic activity of the Co-Ni/BP for the OER.

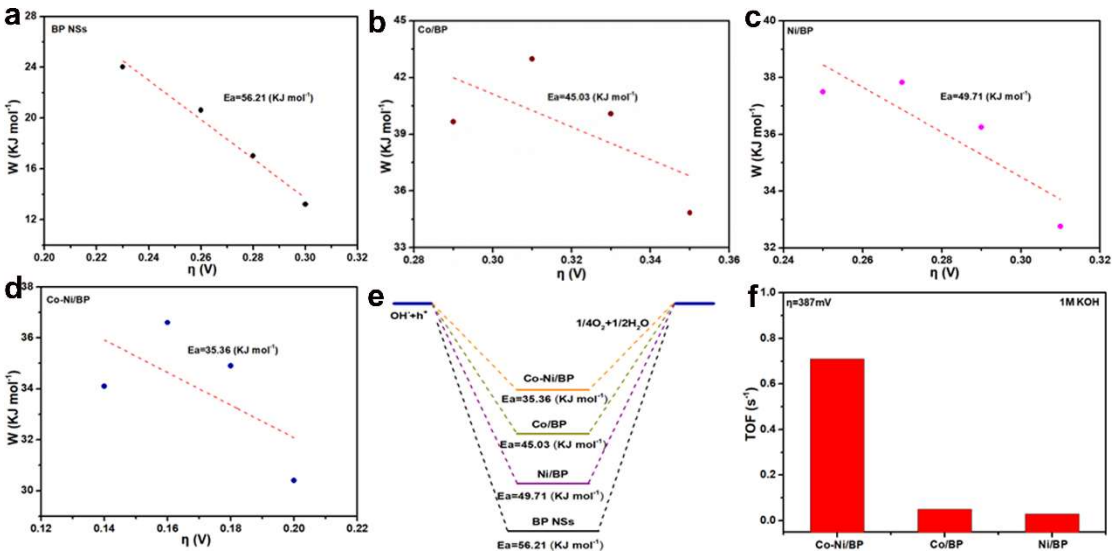

Fig. 9 Typical Arrhenius plots for the BP NSs (a), Co/BP (b), Ni/BP (c), Co-Ni/BP (d) catalysts; corresponding comparative E_a values (e); TOF values (f) of the Co/BP, Ni/BP and Co-Ni/BP catalysts.

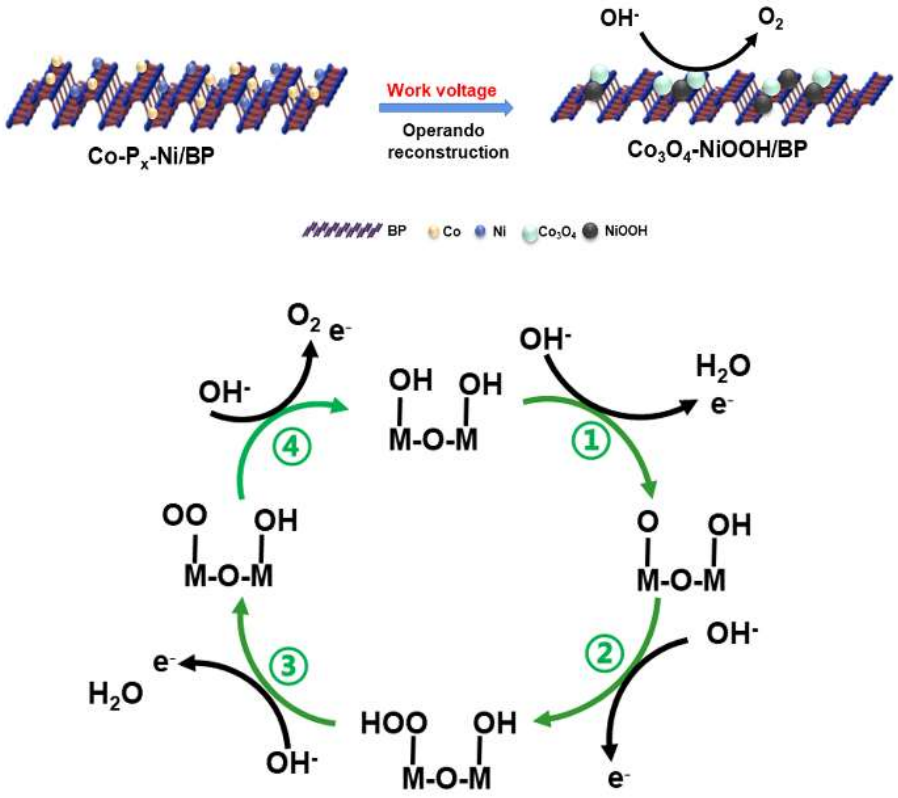

Fig. 10 Proposed theoretical models (upper) and steps (lower) for OER reaction over Co-Ni/BP.

As discussed, the pre-catalyst of Co-Ni/BP was synthesized by a facile electrochemical process with raw materials of bulky BP, a Co wire and a Ni wire. The characterization and OER activity results suggest the initial active centers of the Co-Ni/BP catalyst are Co^{2+} and Ni^{2+} sites. These sites form into a Ni-P_x-Co heterostructure, where electrons transfer from the Ni species to a Co species *via* a P bridge. During the OER process, the OH^- species are adsorbed on Co^{2+} and Ni^{2+} sites and evolve into OH*. Meanwhile, Co^{2+} and Ni^{2+} sites are converted into Co^{3+} and Ni^{3+} sites, which supports the real active sites for OER and contributes to superior OER performance (**Fig. 10**). It means metal sites contribute to OER activity rather than lattice oxygen. Thus, here the OER pathway is followed by AEM mechanism. As

a typical OER process, it contains a continuous process of OH*-O*-OOH*-O_2. OH^- species first adsorb on the active sites. Then the adsorbed OH (HO* species) experiences subsequent deprotonation to form O*. The following step of O-O bond formation makes O* react with another OH^- to generate the HOO* intermediate. In the final step, O_2 is evolved by deprotonation of HOO* with the regeneration of the active site. The reconstruction of the Co-Ni/BP catalyst not only regulates the adsorption strength of OH*, but also makes RDS converted from an electron transfer process or a chemical reaction process to an electron-proton reaction. In this way, the activation energy of whole reaction is reduced, and the OER activity is promoted.

4. Conclusion

In summary, the Co-Ni/BP catalyst has been synthesized by a facile electrolysis-solvothermal process. It shows high OER performance, such as low overpotential and high stability. More importantly, operando reconstruction of the Co-Ni/BP catalyst has been revealed. Before the OER test, the original Ni-P_x-Co structure was formed, where electrons are transferred from the Ni species to the Co species *via* P bridge. After the OER test, Ni_2P is formed into NiOOH and CoP into Co_3O_4, where a heterogeneous structure of Co_3O_4-NiOOH is generated. The original active sites of the Co-Ni/BP catalyst are the Co^{2+}-Ni^{2+} dual-sites before the OER, which evolving into Co^{3+}-Ni^{3+} dual-sites after the OER. This formed heterostructure of Co_3O_4-NiOOH efficiently adjusts electronic structures of both Co and Ni sites, then optimizes the adsorption performance, namely the appropriate adsorption ability

toward OH* intermediates. This makes the RDS of the OER converted from an electron transfer process or a chemical reaction process to an electron-proton reaction. Therefore, this work might shed some new insights into operando reconstruction of the Co-Ni/BP catalyst on its catalytic activity toward the OER. It is expected to be a new way to design efficient BP-based heterostructures for the OER.

Acknowledgement

This research was supported by the National Natural Science Foundation of China (21571119), Fundamental Research Program of Shanxi Province (No. 202203021221130, No. 202203021221136, No. 20210302124473), the Natural Science Foundation of Shanxi Province (No. 202203021221130, No. 202203021221136, No. 20210302124473), "Chunhui Plan" Cooperative Scientific Research Project of Education Ministry (No. HZKY20220510), Scientific and Technological Innovation Programs of Higher Education Institution in Shanxi (2019L0466), the Graduate Education Innovation Project of Shanxi Province (2021Y480, 2022Y483), the China postdoctoral Science Foundation (2021M691366), the Graduate Education Innovation Project of Shanxi Normal University (2021XSY038) and 1331 Engineering of Shanxi Province.

Reference:

[1] Shi Q, Zhu C, Du D, Lin Y. Robust noble metal-based electrocatalysts for oxygen evolution reaction. Chem Soc Rev 2019;48:3181–92. https://doi.org/10.1039/c8cs00671g.

[2] Zhou Y, Sun S, Wei C, Sun Y, Xi P, Feng Z, et al. Significance of Engineering

the Octahedral Units to Promote the Oxygen Evolution Reaction of Spinel Oxides. Adv Mater 2019;31:1–11. https://doi.org/10.1002/adma.201902509.

[3] Yuan Z, Li J, Yang M, Fang Z, Jian J, Yu D, et al. Ultrathin Black Phosphorus-on-Nitrogen Doped Graphene for Efficient Overall Water Splitting: Dual Modulation Roles of Directional Interfacial Charge Transfer. J Am Chem Soc 2019;141:4972–9. https://doi.org/10.1021/jacs.9b00154.

[4] Jiang Q, Xu L, Chen N, Zhang H, Dai L, Wang S. Facile Synthesis of Black Phosphorus: an Efficient Electrocatalyst for the Oxygen Evolving Reaction. Angew Chemie Int Ed 2016;55:13849–53. https://doi.org/10.1002/anie.201607393.

[5] Zeng Y, Zhao M, Huang Z, Zhu W, Zheng J, Jiang Q, et al. Surface Reconstruction of Water Splitting Electrocatalysts. Adv Energy Mater 2022;12:1–29. https://doi.org/10.1002/aenm.202201713.

[6] Wang YZ, Yang M, Ding YM, Li NW, Yu L. Recent Advances in Complex Hollow Electrocatalysts for Water Splitting. Adv Funct Mater 2022;32:1–19. https://doi.org/10.1002/adfm.202108681.

[7] Xiao H, Du X, Zhao M, Li Y, Hu T, Wu H, et al. Structural dependence of electrosynthesized cobalt phosphide/black phosphorus pre-catalyst for oxygen evolution in alkaline media. Nanoscale 2021;13:7381–8. https://doi.org/10.1039/D1NR00062D.

[8] Zhao M, Cheng X, Xiao H, Gao J, Xue S, Wang X, et al. Cobalt-iron oxide/black phosphorus nanosheet heterostructure: Electrosynthesis and performance of (photo-)electrocatalytic oxygen evolution. Nano Res 2023;16:6057–66. https://doi.org/10.1007/s12274-022-4676-9.

[9] Xiao H, Zhang R, Zhao M, Yang X, Jing Y, Zhang L, et al. 2D/1D heterostructure of carbon nanotubes wrapping black phosphorus nanosheets with superior electrophilic property for improving oxygen evolution reaction. Int J Hydrogen Energy 2023;48:18685–95. https://doi.org/10.1016/j.ijhydene.2023.01.373.

[10] Xiang W, Yang N, Li X, Linnemann J, Hagemann U, Ruediger O, et al. 3D atomic-scale imaging of mixed Co-Fe spinel oxide nanoparticles during oxygen evolution reaction. Nat Commun 2022;13:1–14. https://doi.org/10.1038/s41467-021-27788-2.

[11] Kim BJ, Fabbri E, Abbott DF, Cheng X, Clark AH, Nachtegaal M, et al.

Functional Role of Fe-Doping in Co-Based Perovskite Oxide Catalysts for Oxygen Evolution Reaction. J Am Chem Soc 2019;141:5231–40. https://doi.org/10.1021/jacs.8b12101.

[12] Zhu Y, Tahini HA, Hu Z, Chen ZG, Zhou W, Komarek AC, et al. Boosting Oxygen Evolution Reaction by Creating Both Metal Ion and Lattice-Oxygen Active Sites in a Complex Oxide. Adv Mater 2020;32:1–8. https://doi.org/10.1002/adma.201905025.

[13] Noreen S, Tahir MB, Hussain A, Nawaz T, Rehman JU, Dahshan A, et al. Emerging 2D-Nanostructured materials for electrochemical and sensing Application-A review. Int J Hydrogen Energy 2022;47:1371–89. https://doi.org/10.1016/j.ijhydene.2021.10.044.

[14] Rizk MR, Abd El-Moghny MG, Abdelhady HH, Ragheb WM, Mohamed AH, Fouad HF, et al. Tailor-designed bimetallic Co/Ni macroporous electrocatalyst for efficient glycerol oxidation and water electrolysis. Int J Hydrogen Energy 2022;47:32145–57. https://doi.org/10.1016/j.ijhydene.2022.07.129.

[15] Qureshi F, Yusuf M, Pasha AA, Khan HW, Imteyaz B, Irshad K. Sustainable and energy efficient hydrogen production via glycerol reforming techniques: A review. Int J Hydrogen Energy 2022;47:41397–420. https://doi.org/10.1016/j.ijhydene.2022.04.010.

[16] Raj SK, Bhadu GR, Upadhyay P, Kulshrestha V. Three-dimensional Ni/Fe doped graphene oxide @ MXene architecture as an efficient water splitting electrocatalyst. Int J Hydrogen Energy 2022;47:41772–82. https://doi.org/10.1016/j.ijhydene.2022.05.204.

[17] Gao L, Cui X, Sewell CD, Li J, Lin Z. Recent advances in activating surface reconstruction for the high-efficiency oxygen evolution reaction. Chem Soc Rev 2021;50:8428–69. https://doi.org/10.1039/d0cs00962h.

[18] He Q, Wan Y, Jiang H, Pan Z, Wu C, Wang M, et al. Nickel Vacancies Boost Reconstruction in Nickel Hydroxide Electrocatalyst. ACS Energy Lett 2018;3:1373–80. https://doi.org/10.1021/acsenergylett.8b00515.

[19] Ji P, Yu R, Wang P, Pan X, Jin H, Zheng D, et al. Ultra-Fast and In-Depth Reconstruction of Transition Metal Fluorides in Electrocatalytic Hydrogen Evolution Processes. Adv Sci 2022;9. https://doi.org/10.1002/advs.202103567.

[20] Jin H, Xin S, Chuang C, Li W, Wang H, Zhu J, et al. Black phosphorus composites with engineered interfaces for high-rate high-capacity lithium

storage. Science 2020;370:192–7. https://doi.org/10.1126/science.aav5842.

[21] Sun H, Tung CW, Qiu Y, Zhang W, Wang Q, Li Z, et al. Atomic Metal-Support Interaction Enables Reconstruction-Free Dual-Site Electrocatalyst. J Am Chem Soc 2022;144:1174–86. https://doi.org/10.1021/jacs.1c08890.

[22] Wang Z, Zhou Y, Xia C, Guo W, You B, Xia BY. Efficient Electroconversion of Carbon Dioxide to Formate by a Reconstructed Amino-Functionalized Indium–Organic Framework Electrocatalyst. Angew Chem Int Ed 2021;60:19107–12. https://doi.org/10.1002/anie.202107523.

[23] Xu Z, Chen Q, Chen Q, Wang P, Wang J, Guo C, et al. Interface enables faster surface reconstruction in a heterostructured Co-Ni-S electrocatalyst towards efficient urea oxidation. J Mater Chem A 2022;16. https://doi.org/10.1039/d2ta05494a.

[24] Zhao D, Zhang R, Dai M, Liu H, Jian W, Bai FQ, et al. Constructing High Efficiency CoZnxMn2–xO4 Electrocatalyst by Regulating the Electronic Structure and Surface Reconstruction. Small 2022;18. https://doi.org/10.1002/smll.202107268.

[25] Liu X, Guo R, Huang W, Zhu J, Wen B, Mai L. Advances in Understanding the Electrocatalytic Reconstruction Chemistry of Coordination Compounds. Small 2021;17:1–28. https://doi.org/10.1002/smll.202100629.

[26] Liu X, Guo R, Ni K, Xia F, Niu C, Wen B, et al. Reconstruction-Determined Alkaline Water Electrolysis at Industrial Temperatures. Adv Mater 2020;32. https://doi.org/10.1002/adma.202001136.

[27] Liu X, Meng J, Ni K, Guo R, Xia F, Xie J, et al. Complete Reconstruction of Hydrate Pre-Catalysts for Ultrastable Water Electrolysis in Industrial-Concentration Alkali Media. Cell Reports Phys Sci 2020;1. https://doi.org/10.1016/j.xcrp.2020.100241.

[28] Liu X, Meng J, Zhu J, Huang M, Wen B, Guo R, et al. Comprehensive Understandings into Complete Reconstruction of Precatalysts: Synthesis, Applications, and Characterizations. Adv Mater 2021;33. https://doi.org/10.1002/adma.202007344.

[29] Liu X, Ni K, Wen B, Guo R, Niu C, Meng J, et al. Deep Reconstruction of Nickel-Based Precatalysts for Water Oxidation Catalysis. ACS Energy Lett 2019;4:2585–92. https://doi.org/10.1021/acsenergylett.9b01922.

[30] Liu X, Ni K, Wen B, Niu C, Meng J, Guo R, et al. Polyoxomolybdate-derived carbon-encapsulated multicomponent electrocatalysts for synergistically boosting hydrogen evolution. J Mater Chem A 2018;6:17874–81. https://doi.org/10.1039/c8ta07135g.

[31] Mei J, Shang J, He T, Qi D, Kou L, Liao T, et al. 2D/2D Black Phosphorus/Nickel Hydroxide Heterostructures for Promoting Oxygen Evolution via Electronic Structure Modulation and Surface Reconstruction. Adv Energy Mater 2022;12:2201141. https://doi.org/10.1002/aenm.202201141.

[32] Wang S, Song C, Cai Y, Li Y, Jiang P, Li H, et al. Interfacial Polarization Triggered by Covalent-Bonded MXene and Black Phosphorus for Enhanced Electrochemical Nitrate to Ammonia Conversion. Adv Energy Mater 2023;13. https://doi.org/10.1002/aenm.202301136.

[33] Anand R, Nissimagoudar AS, Umer M, Ha M, Zafari M, Umer S, et al. Late Transition Metal Doped MXenes Showing Superb Bifunctional Electrocatalytic Activities for Water Splitting via Distinctive Mechanistic Pathways. Adv Energy Mater 2021;11:1–11. https://doi.org/10.1002/aenm.202102388.

[34] Liang T, Lenus S, Liu Y, Chen Y, Sakthivel T, Chen F, et al. Interface and M3+/M2+ Valence Dual-Engineering on Nickel Cobalt Sulfoselenide/Black Phosphorus Heterostructure for Efficient Water Splitting Electrocatalysis. Energy Environ Mater 2023;6:1–10. https://doi.org/10.1002/eem2.12332.

[35] Guo J, Gan W, Ding C, Lu Y, Li J, Qi S, et al. Black phosphorus quantum dots and Ag nanoparticles co-modified TiO2 nanorod arrays as powerful photocatalyst for tetracycline hydrochloride degradation: Pathways, toxicity assessment, and mechanism insight. Sep Purif Technol 2022;297:121454. https://doi.org/10.1016/j.seppur.2022.121454.

[36] Zhang L, Wang ZQ, Liao J, Zhang X, Feng D, Deng H, et al. Infrared-to-visible energy transfer photocatalysis over black phosphorus quantum dots/carbon nitride. Chem Eng J 2022;431:133453. https://doi.org/10.1016/j.cej.2021.133453.

[37] Shi F, Geng Z, Huang K, Liang Q, Zhang Y, Sun Y, et al. Cobalt Nanoparticles/Black Phosphorus Nanosheets: An Efficient Catalyst for Electrochemical Oxygen Evolution. Adv Sci 2018;5:1800575. https://doi.org/10.1002/advs.201800575.

[38] Chen H, Chen J, Ning P, Chen X, Liang J, Yao X, et al. 2D Heterostructure of

Amorphous CoFeB Coating Black Phosphorus Nanosheets with Optimal Oxygen Intermediate Absorption for Improved Electrocatalytic Water Oxidation. ACS Nano 2021;15:12418–28. https://doi.org/10.1021/acsnano.1c04715.

[39] Li X, Xiao L, Zhou L, Xu Q, Weng J, Xu J, et al. Adaptive Bifunctional Electrocatalyst of Amorphous CoFe Oxide @ 2D Black Phosphorus for Overall Water Splitting. Angew Chem Int Ed 2020;59:21106–13. https://doi.org/10.1002/anie.202008514.

[40] Jiang Q, Xu L, Chen N, Zhang H, Dai L, Wang S. Facile Synthesis of Black Phosphorus: an Efficient Electrocatalyst for the Oxygen Evolving Reaction. Angew Chemie - Int Ed 2016;55:13849–53. https://doi.org/10.1002/anie.201607393.

[41] Budiyanto E, Yu M, Chen M, DeBeer S, Rüdiger O, Tüysüz H. Tailoring Morphology and Electronic Structure of Cobalt Iron Oxide Nanowires for Electrochemical Oxygen Evolution Reaction. ACS Appl Energy Mater 2020;3:8583–94. https://doi.org/10.1021/acsaem.0c01201.

[42] Jin H, Mao S, Zhan G, Xu F, Bao X, Wang Y. Fe incorporated α-Co(OH)2 nanosheets with remarkably improved activity towards the oxygen evolution reaction. J Mater Chem A 2017;5:1078–84. https://doi.org/10.1039/c6ta09959a.

[43] Tao HB, Xu Y, Huang X, Chen J, Pei L, Zhang J, et al. A General Method to Probe Oxygen Evolution Intermediates at Operating Conditions. Joule 2019;3:1498–509. https://doi.org/10.1016/j.joule.2019.03.012.

[44] Xiao H, Yang X, Zhao M, Zhang R, Jing Y, Zhang L, et al. Revealing promotion of interfacial Pt–O–Fe oxygen bridge structure in PtFe/graphene synthesized by a four-electrode electrochemical system on water splitting. Int J Hydrogen Energy 2023;48:38728–41. https://doi.org/10.1016/j.ijhydene.2023.06.200.

[45] Oliver-Tolentino M, Vazquez-Samperio J, Tufiño-Velázquez M, Flores-Moreno J, Lartundo-Rojas L, de R. Bifunctional electrocatalysts for oxygen reduction/evolution reactions derived from NiCoFe LDH materials. J Appl Electrochem 2018;48:947–57. https://doi.org/10.1007/s10800-018-1210-6.